

Solid–solid phase equilibria in the NaCl–KCl system

Jamshed Anwar,^{1, a)} Christian Leitold,^{2, 3, a)} and Baron Peters^{2, 4)}

¹⁾Department of Chemistry, Lancaster University, Lancaster, LA1 4YW, United Kingdom

²⁾Department of Chemical and Biomolecular Engineering, University of Illinois at Urbana-Champaign, Urbana, IL 61801, USA

³⁾Faculty of Physics, University of Vienna, 1090 Wien, Austria (present affiliation)

⁴⁾Department of Chemistry, University of Illinois at Urbana-Champaign, Urbana, IL 61801, USA

(Dated: April 16, 2020)

Solid solutions, structurally ordered but compositionally disordered mixtures, can form for salts, metals, and even organic compounds. The NaCl–KCl system forms a solid solution at all compositions between 657°C and 505°C. Below a critical temperature of 505°C, the system exhibits a miscibility gap with coexisting Na-rich and K-rich rocksalt phases. We calculate the phase diagram in this region using the semi-grand canonical Widom method, which averages over virtual particle transmutations. We verify our results by comparison with free energies calculated from thermodynamic integration and extrapolate the location of the critical point. The calculations reproduce the experimental phase diagram remarkably well and illustrate how solid-solid equilibria and chemical potentials, including those at metastable conditions, can be computed for materials that form solid solutions.

I. INTRODUCTION

Solid solutions are ubiquitous in metallurgy,^{1,2} in geochemistry,^{3,4} in biomineralization,^{5–7} and in many other areas of modern materials science.^{8–13} The atoms in a solid solution reside at regular lattice positions, but the components are randomly intermixed on the lattice. At sufficiently low temperatures, many solid solutions separate into periodic phases with different compositions. Thus solid solutions are nearly perfect realizations of the idealized lattice models that are widely used to study phase transitions in statistical mechanics.^{14,15} At low temperatures, some solid solutions form “coherent precipitates”, i.e. solute-rich precipitates embedded in the surrounding solvent matrix, with both phases sharing one unbroken lattice. Further, certain solid solutions can be quenched to form enormous populations of nanoscale coherent precipitates yielding materials with extraordinary mechanical, magnetic, and heat transfer properties. Examples include precipitate-hardened Ni–Ti–Al superalloys,^{16,17} Heusler or half-Heusler magnetic materials,¹⁸ and radiation resistant alloys for nuclear reactor claddings.^{19,20}

For these materials (and for solids in general), the earliest stages of crystallization, namely, nucleation and subsequent growth, are a major determinant of the structure and hence the properties of the resulting product. Consequently, fundamental studies of nucleation and growth are essential, but challenging both experimentally and theoretically.^{21–23} Notable studies of nucleation and growth in solid solutions have employed Kinetic Monte Carlo simulations.^{24–28} However, rare events like nucleation still pose challenges for kinetic Monte Carlo and molecular simulation. The available empirical po-

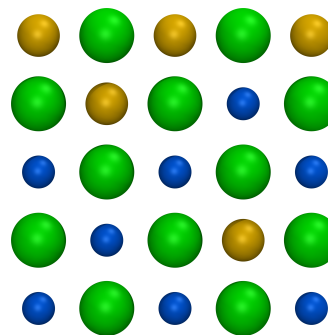


Figure 1. Rendering of a single crystal plane in the NaCl–KCl solid solution. While Cl (green) occupies a regular lattice, Na (blue) and K (yellow) are randomly distributed on the remaining lattice sites. For clarity, thermal fluctuations are not shown.

tentials for multicomponent systems rarely make accurate property predictions while *ab initio* calculations are too costly to capture the statistical ensembles—a sampling issue.²⁹

Simple abstract model systems often yield the most useful and generalizable insights,^{30,31} but it is difficult to quantitatively test their predictions against experiment. This paper investigates a simple but a real model system, a binary mixture of KCl and NaCl salts. Most molten salt mixtures exhibit a sharp eutectic point, without the rather wide and unusual solid solution region seen for NaCl–KCl. In the case of the NaCl–KCl solid solution, the chlorine atoms occupy every other site of a simple cubic lattice, just like in regular rocksalt. The sodium and potassium atoms, which occupy the other half of the rocksalt lattice, are randomly distributed. An illustration of the situation is shown in Fig. 1.

The full phase diagram of the NaCl–KCl system, obtained from the FTsalt database³² that combines multiple experimental results (along with the predicted data

^{a)}J. Anwar and C. Leitold contributed equally to this work.

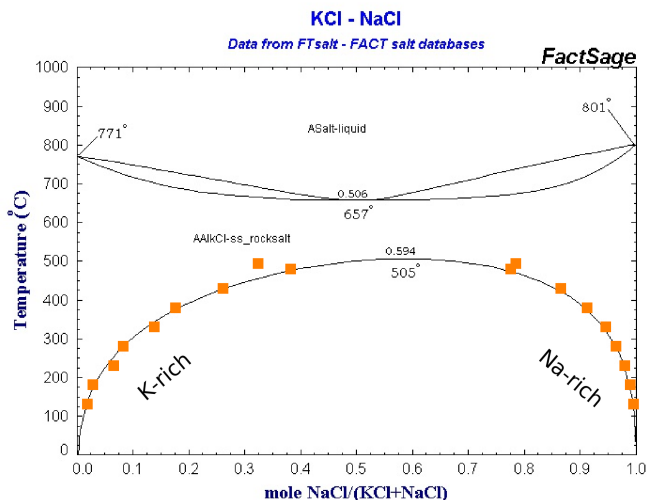


Figure 2. Phase diagram for the NaCl–KCl system (obtained from the FTsalt database³²), which combines multiple experimental results along with the predicted data (orange squares) from the current simulation study.

from the current simulation study) is shown in Fig. 2. The data displayed in the phase diagram was originally compiled by JANAF³³ and has just recently been re-verified experimentally.³⁴ Of particular interest to our study is the fact that for low temperatures, there exists a miscibility gap separating two compositionally different solid solutions, an Na-rich and a K-rich one.

Here we have predicted the Na-rich / K-rich phase envelope in the solid part of the phase diagram using molecular simulation. The calculated phase diagram reproduces the experimental phase diagram remarkably well (Fig. 2). The calculations enable us to predict the difference in chemical potential for NaCl and KCl for any system composition, including the unstable region inside the two-phase envelope.

An important significance of the study is that having an accurate phase diagram now enables *quantitative* theoretical studies of nucleation to be carried out for this model, as the chemical potential is now accurately defined rather than assumed being equal to experimental data. Theoretical models invariably show divergence from experimental data and the driving force or chemical potential estimated from experimental data can be markedly different from that of the model, introducing significant uncertainty in the calculated nucleation rates.

In predicting the phase diagram we have employed two distinct approaches: (i) the semi-grand canonical approach with the dependent variable being composition as a function of set chemical potential difference, and (ii) Widom’s semi-grand canonical approach involving virtual transmutation of one species to another to determine the chemical potential difference (the dependent variable in this case) as a function of set composition. Whilst we have demonstrated that both approaches give consistent results, the Widom’s semi-grand approach

has significant advantages and hence was our method of choice. We introduce the computational model in Section II A, outline the regular semi-grand canonical ensemble in Section II B and compare it with semi-grand canonical Widom method in Section II C. Details of the coexistence calculations are presented in Section II D and II E. The results are presented and discussed in Section III followed by concluding remarks in Section IV.

II. MODEL AND METHODS

A. Force field

In order to model the NaCl–KCl system, we employ a Fumi–Tosi³⁵ style force field. The full potential energy is given as a sum of pair terms:

$$U = \sum_{i < j} u(r_{ij}), \quad (1)$$

where

$$u(r_{ij}) = A_{ij} \exp [B_{ij}(\sigma_{ij} - r_{ij})] - \frac{C_{ij}}{r_{ij}^6} - \frac{D_{ij}}{r_{ij}^8} + \frac{1}{4\pi\epsilon_0} \frac{q_i q_j}{r_{ij}}, \quad (2)$$

and r_{ij} is the distance between particles i and j . The parameters A_{ij} , B_{ij} , C_{ij} , D_{ij} , and σ_{ij} are specific for the combination of elements of particles i and j and hence there are six sets of parameters for all the possible element pairings. These parameters, shown in Table I, are based on those given by Adams and MacDonald.³⁶

The final term in the force field is the electrostatic interaction, where the charges (in units of the elementary charge q_e) are +1 on Na and K and -1 on Cl. With the system of units employed in this study, $(4\pi\epsilon_0)^{-1} = 1389.35 \text{ kJ/mol } \text{\AA}^2 q_e^{-2}$, where ϵ_0 is the permittivity of free space.

Interestingly, in the parameter set tabulated by Adams and MacDonald,³⁶ the Cl–Cl C parameter for Cl in NaCl ($6985.70 \text{ \AA}^6 \text{ kJ mol}^{-1}$) is different from that for Cl in KCl ($7497.60 \text{ \AA}^6 \text{ kJ mol}^{-1}$). Here we have utilised the average of these two parameter values. The same is true for the Cl–Cl B and D parameters utilised in the present study. For the Na–K hetero-interaction, the σ parameter was taken as the arithmetic mean of the homo-interactions. For the C and D parameters, the commonly employed geometric mean mixing rule was found to be completely inappropriate: for instance, the Na–Cl C parameter obtained from the geometric mean of the Cl–Cl (in NaCl) and Na–Na C parameters yielded a value that was almost 25% larger than the specified Na–Cl C parameter tabulated by Adams and MacDonald.³⁶ On searching the literature we came across the alternative mixing rule proposed by Thakkar,³⁷

$$C_{ij} = \frac{2\alpha_i\alpha_j C_i C_j}{\alpha_i^2 C_i + \alpha_j^2 C_j}, \quad (3)$$

where α_i are (dimensionless) polarisabilities. Thakkar’s rule reproduced the Na–Cl C and D interaction parameters using polarisabilities taken from Mayer³⁸ with no more than 4% deviation or better. Consequently the Na–K C and D parameters were estimated with Thakkar’s mixing rule using the polarisabilities of $\alpha_{\text{Na}}=0.1820$ and $\alpha_{\text{K}}=0.8443$ from Mayer.³⁸

	A	B	C	D	σ
	kJ/mol	\AA^{-1}	\AA^6 kJ/mol	\AA^8 kJ/mol	\AA
Na–Na	25.444	3.155	101.17	48.18	2.340
Na–Cl	20.355	3.155	674.48	837.08	2.755
Cl–Cl	15.266	3.061	7241.65	14543.47	3.170
K–K	25.444	2.967	1463.38	1445.31	2.926
K–Na	25.444	3.061	377.31	260.28	2.633
K–Cl	20.355	2.967	2890.63	4396.16	3.048

Table I. Force field parameters for NaCl–KCl.

B. Semi-grand canonical ensemble simulation

Fluid-fluid phase equilibria require thermal, mechanical, and compositional equilibrium, i.e. $T = T_1 = T_2$, $p = p_1 = p_2$, and $\mu(x_1, T, p) = \mu(x_2, T, p)$. If one can guess the approximate fluid densities and a composition between x_1 and x_2 , then the equilibrium conditions can often be identified from a simple direct coexistence simulation. A system held at T , p , and intermediate overall composition will spontaneously split into two phases, one at composition x_1 separated by an interface from another at composition x_2 . In a long thin simulation box with fixed cross section and pressure applied from the ends, the interface spontaneously forms perpendicular to the long axis such that surface tension exerts no pressure on the adjacent “bulk” phases. If the box is much longer than the interface thickness, the equilibrium compositions can then be estimated from the simulated concentration profiles.^{39–41} Similar direct coexistence simulations have been used to estimate solubilities of certain solids.^{42–45} An alternative collection of indirect Monte Carlo techniques, which have found widespread application, can identify phase coexistence conditions without ever simulating the interface between phases or guessing approximate densities and compositions. These include grand canonical ensemble simulations,^{46,47} the Gibbs ensemble simulations,⁴⁸ Gibbs-Duhem integration,^{49,50} density of states methods,^{51,52} and osmotic ensemble Monte Carlo simulations.⁵³

For multicomponent solid-solid equilibria, the same conditions apply at equilibrium. However, additional difficulties require methods beyond those used for fluid-fluid and fluid-solid equilibria. First, a dense crystalline solid with no vacancies has no free space for inserting or growing new particles, thus preventing the use of grand

canonical simulations, osmotic ensemble simulations, and Gibbs-ensemble simulations with particle insertions. Second, a simulated periodic crystal has allowed volumes that are effectively discretized by the need to complete integer layers of the crystal, thus also preventing the use of Gibbs ensemble simulations with particle exchanges. Third, two solids in direct contact with each other exert stresses on the neighboring phase,⁵⁴ especially when they share a coherent interface as expected for KCl inclusions in NaCl or NaCl inclusions in KCl. These stresses cause long range strain (lattice distortion) in the two solids. The stresses and strains can alter equilibrium compositions,⁵⁵ so direct solid-solid coexistence simulations are also not an option.

To enable the calculation of multicomponent solid-solid equilibria, we explore the semi-grand approach by Kofke and Glandt,⁵⁶ where particles are transmuted into alternative species instead of being inserted. The acceptance probability depends on the chemical potential *difference* between the species, rather than the individual chemical potentials. For the binary solid solution, the semi-grand approach therefore yields the required composition ratio as function of defined chemical potential difference $\Delta\mu = \mu_B - \mu_A$.

We utilised the semi-grand ensemble for the NaCl–KCl solid solution to determine co-existence compositions at a number of temperatures, but found this strategy cumbersome and inefficient compared with the Widom’s semi-grand approach detailed in Sec. II C.

C. Semi-grand canonical Widom simulation

The test particle method originally introduced by Widom⁵⁷ directly probes the excess chemical potential of a substance in a simulation. In the case of a system of N identical particles of mass m at pressure p and temperature T the isothermal-isobaric partition function is

$$Z_{NpT} \equiv \frac{\beta p}{h^{3N} N!} \int_0^\infty dV e^{-\beta p V} \int dr^N dp^N e^{-\beta H(r^N, p^N)}, \quad (4)$$

where $H(r^N, p^N)$ is the system’s Hamiltonian, $\beta = 1/k_B T$, k_B is the Boltzmann constant, and h is Planck’s constant. The chemical potential μ can be calculated from

$$\beta\mu = \frac{\partial}{\partial N} [-\ln Z_{NpT}]. \quad (5)$$

The Hamiltonian is

$$H(r^N, p^N) = \sum_{i=1}^N \frac{p_i^2}{2m} + U(r^N), \quad (6)$$

so we can split μ into an ideal and excess part,

$$\mu = \mu^{\text{id}} + \mu^{\text{ex}}. \quad (7)$$

The ideal part is given by setting $U(r^N) = 0$, explicitly performing the momentum integrals, and then applying Eq. (5),

$$e^{-\beta\mu^{\text{id}}} \equiv \frac{1}{\beta p \Lambda^3}, \quad (8)$$

where $\Lambda = \sqrt{\beta\hbar^2/2\pi m}$ is the thermal de Broglie wavelength.

For large N , the derivative in Eq. (5) can be substituted by a finite difference $\Delta N = 1$, and the logarithm turns a difference into a ratio of partition functions. One can then show that in the thermodynamic limit we have for the excess part

$$e^{-\beta\mu^{\text{ex}}} = \frac{\beta p \langle V e^{-\beta\Delta U(r_0|r_1, \dots, r_N)} \rangle_N}{N+1}. \quad (9)$$

The average is taken over a uniformly distributed test particle (index 0) in a regular NpT simulation box and the factor in the exponential is the energy change associated with the virtual insertion of this test particle. In the case of an NVT ensemble, Widom's formula reduces to

$$e^{-\beta\mu^{\text{ex}}} = \left\langle e^{-\beta\Delta U(r_0|r_1, \dots, r_N)} \right\rangle_N. \quad (10)$$

While in principle exact, Widom's method in practice suffers from poor convergence in dense systems or crystals.

For multi-component systems, an alternative approach to virtual particle insertions is to average over virtual particle transmutations, as shown by Sindzingre et al.⁵⁸ This makes the method applicable to crystals, enabling the determination of the chemical potential difference for the transmutation of one chemical species to another in the lattice. Consider a two-component system (comprised of components A and B) at temperature T and pressure p . The total particle number is $N = N_A + N_B$. Now, the partition function is

$$Z_{N_A, N_B, p, T} = \beta p \int_0^\infty dV e^{-\beta p V} Z_{N_A, N_B, V, T}, \quad (11)$$

where

$$Z_{N_A, N_B, V, T} = \frac{1}{h^{3N}} \frac{1}{N_A! N_B!} \int dr^N dp^N e^{-\beta H(r^N, p^N)} \quad (12)$$

and the ideal part is given by

$$Z_{N_A, N_B, p, T}^{\text{id}} = \frac{N!}{N_A! N_B!} \frac{1}{(\beta p)^N} \frac{1}{\Lambda_A^{3N_A}} \frac{1}{\Lambda_B^{3N_B}}, \quad (13)$$

where $\Lambda_A = \sqrt{\beta\hbar^2/2\pi m_A}$ is the thermal de Broglie wavelength for species A with mass m_A and Λ_B is defined accordingly. The chemical potential for species A is the derivative

$$\beta\mu_A = -\frac{\partial}{\partial N_A} \ln Z_{N_A, N_B, p, T} = \beta(\mu_A^{\text{id}} + \mu_A^{\text{ex}}), \quad (14)$$

with μ_B defined accordingly.

Consider the difference in chemical potential,

$$\Delta\mu \equiv \mu_B - \mu_A. \quad (15)$$

The ideal component of the chemical potential difference can be calculated analytically,

$$\Delta\mu^{\text{id}} \equiv \mu_B^{\text{id}} - \mu_A^{\text{id}} = -\frac{1}{\beta} \left[\frac{3}{2} \ln \left(\frac{m_B}{m_A} \right) + \ln \left(\frac{N_A}{N_B} \right) \right]. \quad (16)$$

For the excess chemical potential difference, we consider the case when a particle of type A is converted into type B , or vice versa. The difference in excess chemical potential is then directly related to the exponential average of the energy change for the transmutation:

$$\Delta\mu^{\text{ex}} \equiv \mu_B^{\text{ex}} - \mu_A^{\text{ex}} = -\frac{1}{\beta} \ln \left\langle e^{-\beta\Delta U(A^-, B^+)} \right\rangle_{N_A, N_B} \quad (17)$$

$$= \frac{1}{\beta} \ln \left\langle e^{-\beta\Delta U(A^+, B^-)} \right\rangle_{N_A, N_B}. \quad (18)$$

This quantity can be probed using virtual Monte Carlo transmutation moves in an otherwise standard NpT simulation, which itself can be either Monte Carlo or molecular dynamics. It is worth noting that here, the system composition is fixed at (N_A, N_B) while the excess chemical potential difference is the dependent variable. This is in stark contrast to a simulation in the semi-grand canonical ensemble, where one fixes the chemical potential difference and obtains the composition as a result. Note Widom's semi-grand method was used in an earlier study to predict the phase diagram of MgO-MnO solid solution,⁵⁹ but that work refers to the method as a semi-grand canonical simulation.

D. Gibbs free energy from the chemical potential difference

In a binary mixture of species A and B , the full Gibbs free energy *per particle* is given as

$$\hat{G}(N_A, N_B, p, T) = x_A \mu_A + x_B \mu_B, \quad (19)$$

where $x_i = N_i/N$ is the mole fraction of species i , and $\hat{G} = G/N$. Since $x_B = 1 - x_A$, we have

$$\frac{\partial \hat{G}}{\partial x_B} = \mu_B - \mu_A = \Delta\mu, \quad (20)$$

which relates the Gibbs free energy to the chemical potential difference that we obtain from simulations. Using the simplified notation $x := x_B$, one has

$$\hat{G}(x) = \hat{G}_A + \int_0^x dx' \Delta\mu(x'). \quad (21)$$

In other words, but for the reference value \hat{G}_A (the Gibbs free energy of a pure A system), the calculation of $\Delta\mu$

as a function of system composition is sufficient to construct its Gibbs free energy as a function of composition, enabling the determination of co-existence points and hence the binary phase diagram.

In the context of mixtures, the Gibbs free energy is often written in a slightly different form, as

$$\hat{G} = \hat{G}^I + \hat{G}^E. \quad (22)$$

Again, \hat{G} is split into an ideal and excess part, but “ideal” and “excess” in this case have a different meaning. The ideal Gibbs energy is now given as

$$\frac{\hat{G}^I(x)}{k_B T} = (1-x) \frac{\hat{G}_A}{k_B T} + x \frac{\hat{G}_B}{k_B T} + (1-x) \ln(1-x) + x \ln x, \quad (23)$$

where \hat{G}_A and \hat{G}_B describe the pure end states (including all non-idealities in the sense of Sec. II C). The ideal Gibbs energy of the mixture is a composition-weighted linear combination of the pure states plus two mixing entropy terms. This result is consistent with explicitly integrating the ideal gas case, i. e. using Eq. (16) in Eq. (21), and noting that in the special case of two ideal gases that only differ in particle mass, we have

$$\frac{\hat{G}_B}{k_B T} = \frac{\hat{G}_A}{k_B T} - \frac{3}{2} \ln \frac{m_B}{m_A}. \quad (24)$$

Naturally, for any system with non-zero interactions (such as NaCl–KCl), this simple relation between \hat{G}_A and \hat{G}_B does not hold true.

The change of notation is intended here as we want to emphasize that we will in the following assume some functional form for the excess part and fit it to the simulation results. The simplest choice for G^E is called the regular solution model, and is usually written in the form

$$\frac{G^E}{k_B T(1-x)x} = \Omega. \quad (25)$$

The regular solution model is symmetric with respect to A – B interactions, i. e. A in a B solvent has the same G^E as B in an A solvent. The single parameter Ω measures the difference in interaction between the two species. More explicitly,

$$\Omega = N_b \left(\varepsilon_{AB} - \frac{\varepsilon_{AA} + \varepsilon_{BB}}{2} \right), \quad (26)$$

where N_b is the number of bonds per particle and ε_{ij} is the interaction energy of a bond between species i and j . Our results show that a regular solution model is not sufficient for the NaCl–KCl mixture. Asymmetry can be introduced with the two-parameter Margules model,

$$\frac{G^E}{k_B T(1-x)x} = W_1(1-x) + W_2x, \quad (27)$$

which we use to fit our simulation data. Specifically, we combine Eqs. (22), (23), and (27) to get the full Gibbs

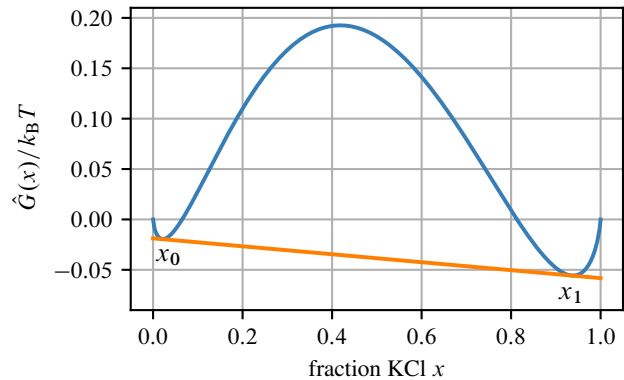


Figure 3. (Blue) Gibbs free energy as a function of composition when there is two-phase coexistence. The data shown are for the NaCl–KCl system at a temperature of 500 K, with x denoting the mole fraction of KCl. Note that the linear part of the Gibbs energy has been subtracted, as this will not affect the final result. (Orange) The double tangent construction yields the coexistence concentrations x_0 and x_1 .

free energy and then take the derivative with respect to x in order to obtain $\Delta\mu$, Eq. (20). The final functional form we use to fit $\Delta\mu(x)$ is hence

$$\frac{\Delta\mu}{k_B T} = W_0 + \ln \left(\frac{x}{1-x} \right) + W_1(1-x)(1-3x) - W_2x[1-3(1-x)], \quad (28)$$

where the parameter $W_0 = (\hat{G}_B - \hat{G}_A)/k_B T$ can be identified as the chemical potential difference of the pure phases. The corresponding Gibbs free energy per particle is

$$\begin{aligned} \frac{\hat{G}(x)}{k_B T} &= xW_0 + (1-x) \ln(1-x) + x \ln(x) \\ &\quad + x(1-x)[W_1(1-x) + W_2x]. \end{aligned} \quad (29)$$

Here, we have used the normalization $\hat{G}_A = 0$. As we will see momentarily, knowledge of the absolute value is not important for the construction of the phase diagram. However, should the Gibbs free energies \hat{G}_A and \hat{G}_B of the pure end states be known, the fitted value of W_0 can serve as a consistency check.

E. Construction of the phase diagram

Consider the Gibbs free energy as a function of system composition as shown in Fig. 3 (blue curve). Two-phase coexistence occurs if this function has a concave region. A homogeneous system with a concentration $x_0 < x < x_1$ is not thermodynamically stable, and the two coexistence concentrations x_0 and x_1 are found with a double tangent construction in the diagram. There, a homogeneous system can lower its free energy by going down to the orange line, the double tangent. Physically, the linear

function corresponds with a system that consists of two separated phases of composition x_0 (A -rich) and x_1 (B -rich), ignoring any interface terms. The double tangent to a function $f(x)$ is found by solving a system of two equations with two unknowns,

$$f'(x_0) = f'(x_1), \quad (30)$$

$$f(x_0) + f'(x_0)(x_1 - x_0) = f(x_1). \quad (31)$$

An important thing to note is that one can replace $f(x)$ by $g(x) = f(x) + kx$, i. e. add an arbitrary linear term, without changing these equations and hence the result for (x_0, x_1) . In practice, almost always the equations have to be solved numerically. To give an example, even in the simple case of a regular solution model, the resulting equation

$$\ln \frac{x}{1-x} = \Omega(2x-1), \quad (32)$$

does not have an algebraic solution.

F. Simulation details

The primary simulations to obtain the phase diagram were carried out using an in-house code, ATOMH.⁶⁰ We also used LAMMPS⁶¹ and DL_POLY⁶² for auxiliary calculations. If not otherwise stated, the system size was $N = 256$ ion pairs, or 512 particles, and the pressure $p = 1$ bar. The cutoff for the non-bonded van der Waals and real-space Coulombic interactions was 0.9 nm. Long range van der Waals corrections were applied to the energy and the virial. The long-range part of the Coulomb interaction was calculated using Ewald summation, with the relative accuracy parameter set to 10^{-6} . For MD simulations, the time step was $\Delta t = 2$ fs. For MC simulations, one sweep corresponded to 512 single-particle moves, and on average 50 exchange moves (Na and K swaps) and 10 volume moves. The quantity of interest, the chemical potential difference $\Delta\mu$, was sampled every 50 sweeps by performing a virtual transmutation of every Na and K atom to the opposite type and updating the corresponding average, Eqs. (17) and (18).

III. RESULTS AND DISCUSSION

A. Force field checks

For a first check of the force field accuracy, we performed simulations of the pure NaCl and KCl crystalline phases, respectively. The average lattice energies at $T = 298$ K were $U(\text{NaCl}) = -769.95 \pm 0.01$ kJ mol⁻¹ per ion-pair, and $U(\text{KCl}) = -700.43 \pm 0.01$ kJ mol⁻¹ per ion-pair, which are in excellent agreement with experimentally determined lattice energies, $U_{\text{expt}}(\text{NaCl}) = -770.3$ kJ mol⁻¹ per ion-pair, and $U_{\text{expt}}(\text{KCl}) = -701.2$ kJ mol⁻¹ per ion-pair.⁶⁴

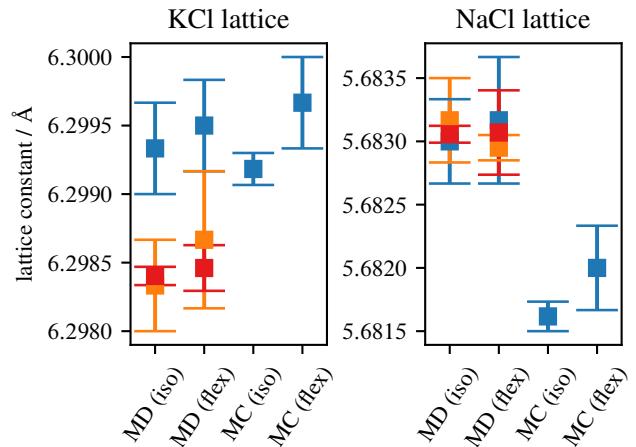


Figure 4. Lattice constants for the pure phases and estimated uncertainties at 298 K. (Blue) ATOMH code results. (Orange) DL_POLY code results. (Red) LAMMPS code results. Iso denotes an isotropic barostat implying a cubic simulation box, and flex a fully flexible box. System size is $N = 864$ ion pairs (1728 particles, 6 unit cells in each direction).

The results for the lattice constants at $T = 298$ K are given in Fig. 4. Accounting for the estimated uncertainty, there is good agreement between both the MC and MD results as well as different simulation packages. There are eight atoms per unit cell, so lattice constant and (number) density are related by $\rho = 8/a^3$. The densities are $\rho(\text{NaCl}) = 0.043595 \pm 0.000007$ Å⁻³ and $\rho(\text{KCl}) = 0.032008 \pm 0.000004$ Å⁻³. The corresponding mass densities are $\rho_m(\text{NaCl}) = 2.1154 \pm 0.0004$ g/cm³ and $\rho_m(\text{KCl}) = 1.9812 \pm 0.0002$ g/cm³. Densities of the mixture as a function of composition for a few other selected temperatures are shown in Fig. 5. In the range of temperatures investigated, there is an approximately linear relationship similar to Vegard's law⁶³ between lattice constant, composition, and temperature:

$$a \approx c_x x + c_T T + a_0. \quad (33)$$

The fitted parameter values are $c_x = 0.62796$ Å, $c_T = 3.1485 \times 10^{-4}$ Å/K, and $a_0 = 5.5911$ Å.

B. Free energies of the pure end states

We calculated the (Helmholtz) free energies of pure NaCl ($x = 0$) and pure KCl ($x = 1$) using the Einstein crystal approach via thermodynamic integration (TI). The calculations closely followed those in a previous work of Anwar, Frenkel, and Noro,⁶⁵ so only a brief overview is given here. The simulations were carried out at a fixed volume corresponding to a pressure of $p = 1$ bar. We used Gauss-Legendre quadrature with $n = 16$ λ nodes for the numerical integration of the free energy derivative $\partial F/\partial\lambda$. The equations are provided in Supporting

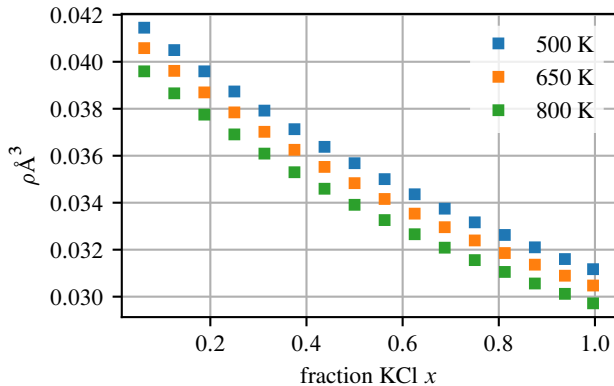


Figure 5. Densities as a function of system composition at three selected temperatures.

Information. In the Einstein crystal part of the calculation, the thermal de Broglie wavelength Λ was set to 1 Å for all species. For the conditions investigated here, the pV term to convert the Helmholtz free energy into a Gibbs free energy is very small and hence deemed unimportant. For example, for NaCl at 298 K, the correction is $pV_{\text{NaCl}}/N_{\text{NaCl}}k_{\text{B}}T \approx 0.001$, much smaller than even the probably slightly underestimated uncertainty in the Helmholtz free energy. The results are summarized in Tab. II.

T	$\hat{F}_{\text{NaCl}}/k_{\text{B}}T$	$\hat{F}_{\text{KCl}}/k_{\text{B}}T$
298	-306.525 ± 0.005	-279.119 ± 0.004
600	-150.766 ± 0.005	-137.474 ± 0.005

Table II. Helmholtz free energies for pure crystalline phases of NaCl and KCl from thermodynamic integration with the thermal de Broglie wavelength set to 1 Å for all species to enable easier comparison with published values of Aragoles, Sanz, and Vega.⁶⁶ In analogy to \hat{G} , \hat{F} denotes the Helmholtz free energy per ion pair.

For NaCl at 298 K, our result is $\hat{F}_{\text{NaCl}}/k_{\text{B}}T = -306.525 \pm 0.005$. The result compares well to that of Aragoles, Sanz, and Vega,⁶⁶ which is $-306.22 k_{\text{B}}T$. Note that these authors report the value *per particle*, while in our study all values are given *per ion pair*, which accounts for the factor two difference to the raw result reported in Tab. II of the reference. As discussed in Sec. II A, the Cl–Cl B , C , and D potential parameters utilized in the present study differ from the Cl–Cl parameters of pure NaCl in the study by Aragoles, Sanz, and Vega. Our B , C , and D parameters are averages from the Cl–Cl parameters for pure NaCl and KCl systems, possibly contributing to the $0.3 k_{\text{B}}T$ difference between our NaCl free energies and theirs.

C. Phase diagram calculation

The miscibility gap is theoretically unstable and inaccessible to regular semigrand canonical simulations, an issue which was noted by Sadigh et al.⁶⁷ Given a fixed $\Delta\mu$, the semigrand canonical simulations always find a composition on either side of the miscibility gap and stay there. Without a good initial guess for the value of $\Delta\mu$ at coexistence, one needs to find it in a tedious, iterative procedure. For example, one can run semigrand simulations with a coarse grid of $\Delta\mu$ values and then iteratively improve the resolution of $\Delta\mu$ at coexistence. Results from this procedure at $T = 600$ K are shown in blue in Fig. 6. This procedure must be repeated for each temperature below the critical point.

Fig. 6 also shows results from Widom’s semi-grand method. While both methods agree on the overall curve, only Widom’s semi-grand method is able to probe the miscibility gap. Furthermore, for the Widom method, the total number of simulations necessary to run is much lower, as the whole curve can be obtained in a single parameter sweep varying the KCl mole fraction from 0 to 1 in equal increments.

For the Widom method, an NaCl–KCl solid solution of any arbitrary composition is unable to undergo phase separation into the two co-existing phases due to interfacial energy barriers, enabling its chemical potential to be monitored. This opportunity of being able to sample the chemical potential of unstable and metastable structures is essential to the application of the double tangent method. So, it appears that the same interfacial barriers that limit the study of phase transition phenomenon by brute force simulation serve here to make the miscibility gap accessible. To confirm that the system does not phase-separate into an Na-rich and a K-rich domain over the full length of our simulations, we carried out spatial and temporal correlation analysis. The analysis and associated results are detailed in Supporting Information and indeed confirm the systems remain homogeneous. For larger systems which do phase-separate, one would need to employ alternative sampling techniques to probe the miscibility gap, such as the generalized replica exchange method developed by Kim, Keyes, and Straub.⁶⁸

Our experience of Widom’s semi-grand approach suggests that this methodology would readily carry over to more complex solid solution systems. There appears to be a remarkable coupling of this method with solid solution phase stability. Convergence of the method requires appreciable overlap of the energy distributions of the original system and that of the virtual perturbed state (when a molecule has been transmuted). This translates to the transmutation energy differences not being excessively large. Phase stability of a solid solution relies on exactly the same energy criteria—the substitution energy difference again must not be too large. The implication is that any system that forms a solid solution is likely to be accessible to Widom’s semi-grand sampling, which would include flexible molecular systems too.

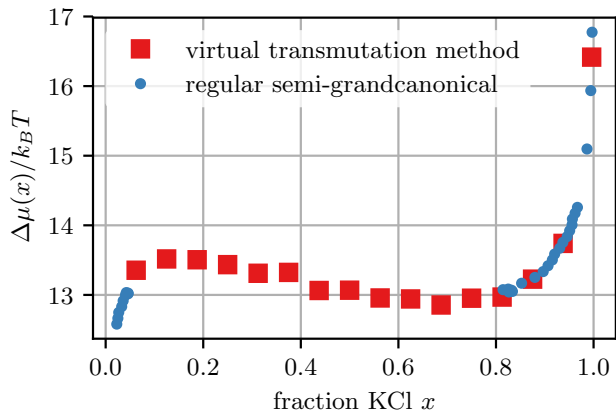


Figure 6. Comparison between a regular semi-grand canonical simulation and the Widom-like virtual transmutation method for NaCl–KCl at $T = 600$ K. It is not possible to access the miscibility gap region with the regular semi-grand method.

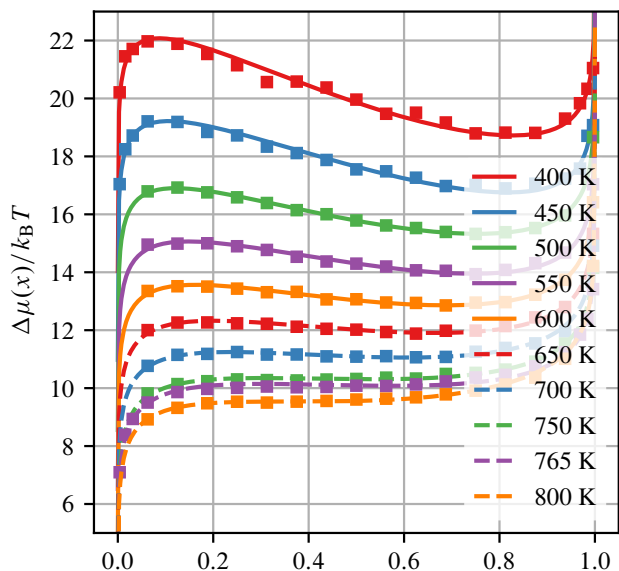


Figure 7. Chemical potential difference for NaCl–KCl at a range of temperatures. x is the fraction of KCl. Each square is the result of a simulation at a fixed composition. The lines are fits with Eq. (28).

We have performed simulations covering the full range of compositions for multiple temperatures (Fig. 7). The obtained fit parameters W_1 and W_2 are used to find the corresponding coexistence concentrations x_0 and x_1 via a double tangent construction. The highest temperature, 800 K, is above the critical point. This is already obvious from the functional form of $\Delta\mu(x)$, which is strictly monotonic. Consequently, the corresponding Gibbs free energy is convex, and no phase coexistence occurs. The results for (x_0, x_1) are shown in Fig. 2 and plotted on

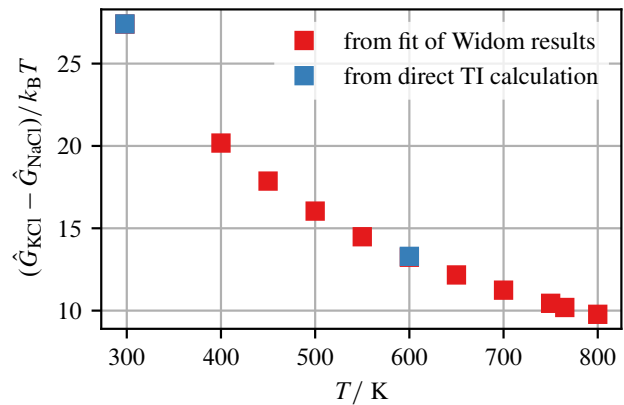


Figure 8. Gibbs free energy difference between the pure phases obtained from the fitting constant W_0 and from independent Einstein crystal-based calculations for the pure phases. For $T = 298$ K, the two results are so close that only the topmost marker (blue) is visible.

top of the experimental phase diagram from the literature. Note that in this figure, the x axis denotes the mole fraction of NaCl. The accuracy of the prediction is remarkable, highlighting the quality of the NaCl–KCl forcefield, validating Thakkar’s mixing rule,³⁷ and the power of Widom’s semi-grand simulation protocol. The largest deviations between the experimental results and the ones computed in this study appear at higher temperatures near the critical point. Presumably, this is due to larger fluctuations in the vicinity of the critical point, which make it harder for the computational results to converge.

To verify the consistency of our simulations, we show the results for the Gibbs free energy difference between the two pure phases ($\hat{G}_{\text{KCl}} - \hat{G}_{\text{NaCl}}$) as a function of temperature in Fig. 8. The data shown here is derived from both the independently determined free energies of the pure end states and from the semi-grand canonical Widom simulations. For the Widom simulations the free energy difference corresponds directly to the value of the fit parameter W_0 . The free energies of the pure KCl and NaCl are those calculated using thermodynamic integration starting from an Einstein crystal at $T = 298$ K and $T = 600$ K. As seen in the figure, we have almost perfect agreement between the two methods. Note that the semi-grand canonical Widom results for $T = 298$ K are not shown in Fig. 7, we use them only for the consistency check.

D. Critical point extrapolation

We use Guggenheim’s empirical formula⁶⁹ to extrapolate the critical point. The original formula is for the critical point in a gas-liquid transition of argon, and it gives the gas (ρ_g) and liquid (ρ_l) densities as a function

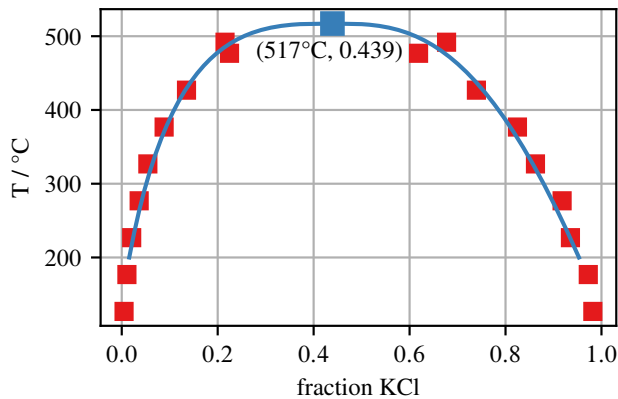


Figure 9. Extrapolated critical point for NaCl–KCl using the Guggenheim formula, Eqs. (34) and (35). The red data points are the same as shown in Fig. 2, but note that the x-axis is reversed compared to Fig. 2.

of temperature:

$$\frac{\rho_l}{\rho_c} = 1 + 0.75 \left(\frac{T_c - T}{T_c} \right) + 1.75 \left(\frac{T_c - T}{T_c} \right)^{1/3}, \quad (34)$$

$$\frac{\rho_g}{\rho_c} = 1 + 0.75 \left(\frac{T_c - T}{T_c} \right) - 1.75 \left(\frac{T_c - T}{T_c} \right)^{1/3}. \quad (35)$$

The critical point is (T_c, ρ_c) . In the present application, mole fraction x is substituted for the density. We allow both the critical point as well as the numerical parameters 0.75 and 1.75 to change in order to give the best fit to our data. The result is shown in Fig. 9.

IV. CONCLUDING REMARKS

We have demonstrated that the semi-grand canonical Widom method⁵⁸ can accurately and efficiently compute the phase diagram for a multicomponent solid as a function of temperature and composition. Specifically, we have computed the binodal for solid solutions of Tosi–Fumi NaCl and KCl below the critical temperature. We used the semi-grand Widom framework to compute the chemical potential difference between NaCl and KCl components as a function of composition. The chemical potential data were converted to ideal and excess free energies, fitted to a Margules model, and then used to determine coexistence compositions by common tangent constructions.

Our results are in remarkable agreement with the phase diagram based on experimental data, a testament to the Fumi–Tosi force field, Thakkar’s mixing rule, and the robust convergence of the Widom’s semi-grand method. Perhaps more importantly, our results provide coexistence conditions and chemical potentials at metastable compositions within the binodal. Thus the results open

the door to quantitative studies of nucleation, growth, and coarsening processes within solid solutions.

V. SUPPLEMENTARY MATERIAL

In the Supplementary Material, we provide details on the thermodynamic integration procedure to calculate the free energies of the pure salts and provide absolute free energy results using the true thermal de Broglie wavelengths. We also compare our version of the Cl–Cl interaction with the one used in earlier studies and show the lattice parameter of the mixture for different temperatures. Furthermore, we perform a spatial and temporal correlation analysis to ensure compositional homogeneity throughout the unstable zone of the phase diagram.

VI. ACKNOWLEDGMENTS

BP and CL acknowledge financial support from the National Science Foundation Award No. 1465289 in the Division of Theoretical Chemistry. We thank Mikhail Laventiev, Kartik Kamat, and Daan Frenkel for helpful discussions.

REFERENCES

- ¹D. A. Porter and K. E. Easterling, *Phase Transformations in Metals and Alloys* (Springer, London, 1992).
- ²W. Kurz and D. J. Fisher, *Fundamentals of solidification*, 4th ed. (Trans Tech Publications, Zürich, 1998).
- ³A. Putnis, *An Introduction to Mineral Sciences* (Cambridge University Press, Cambridge, 1992).
- ⁴U. Becker and M. Prieto, *Chemical Geology* **225**, 173 (2006).
- ⁵L. Addadi, S. Raz, and S. Weiner, *Advanced Materials* **15**, 959 (2003).
- ⁶A. Becker, A. Ziegler, and M. Epple, *Dalton Transactions* 1814 (2005).
- ⁷K. E. Chave, *The Journal of Geology* **60**, 190 (1952).
- ⁸M. D. Graef and M. E. McHenry, *Structure of Materials: An Introduction to Crystallography, Diffraction, and Symmetry* (Cambridge University Press, Cambridge, 2007).
- ⁹J. C. Mikkelsen Jr. and J. B. Boyce, *Physical Review Letters* **49**, 1412 (1982).
- ¹⁰G. Joshi *et al.*, *Nano Letters* **8**, 4670 (2008).
- ¹¹J. Androulakis *et al.*, *Journal of the American Chemical Society* **129**, 9780 (2007).
- ¹²R. E. Eitel, C. A. Randall, T. R. Shrout, and S. E. Park, *Japanese Journal of Applied Physics* **41**, 2099 (2002).
- ¹³E. P. George, D. Raabe, and R. O. Ritchie, *Nature Reviews Materials* **4**, 515 (2019).
- ¹⁴D. Chandler, *Introduction to Modern Statistical Mechanics* (Oxford University Press, Oxford, 1987).
- ¹⁵H. E. Stanley, *Introduction to Phase Transitions and Critical Phenomena* (Oxford University Press, Oxford, 1987).
- ¹⁶A. G. Khachatryan, *Theory of Structural Transformations in Solids, Dover Books on Engineering Series* (Dover Publications, Mineola, 2008).
- ¹⁷T. M. Pollock and A. S. Argon, *Acta Metallurgica Et Materialia* **42**, 1859 (1994).
- ¹⁸Y. W. Chai and Y. Kimura, *Acta Materialia* **61**, 6684 (2013).

- ¹⁹G. R. Odette, M. J. Alinger, and B. D. Wirth, *Annual Review of Materials Research* **38**, 471 (2008).
- ²⁰M. K. Miller, B. D. Wirth, and G. R. Odette, *Materials Science and Engineering A* **353**, 133 (2003).
- ²¹*Nucleation: A transition state to the directed assembly of materials*, in *Faraday Discussions*, Vol. 179 (Royal Society of Chemistry, Cambridge, 2015).
- ²²P. G. Vekilov, *Crystal Growth and Design* **10**, 5007 (2010).
- ²³J. Anwar and D. Zahn, *Angewandte Chemie International Edition* **50**, 1996 (2011).
- ²⁴H. Wu, T. Mayeshiba, and D. Morgan, *Scientific Data* **3**, 1 (2016).
- ²⁵Y. Zhang, X. M. Bai, J. Yu, M. R. Tonks, M. J. Noordhoek, and S. R. Phillpot, *Acta Materialia* **111**, 357 (2016).
- ²⁶E. Clouet, L. Laé, T. Épicier, W. Lefebvre, M. Nastar, and A. Deschamps, *Nature Materials* **5**, 482 (2006).
- ²⁷J. Marian and V. V. Bulatov, *Journal of Nuclear Materials* **415**, 84 (2011).
- ²⁸J. H. Ke, H. Ke, G. R. Odette, and D. Morgan, *Journal of Nuclear Materials* **498**, 83 (2018).
- ²⁹S. Curtarolo, D. Morgan, and G. Ceder, *Calphad: Computer Coupling of Phase Diagrams and Thermochemistry* **29**, 163 (2005).
- ³⁰M. Athènes, P. Bellon, and G. Martin, *Acta Materialia* **48**, 2675 (2000).
- ³¹R. LeSar, *Introduction to Computational Materials Science* (Cambridge University Press, Cambridge, 2013).
- ³²C. Bale *et al.*, *Calphad* **26**, 189 (2002).
- ³³M. W. Chase, C. A. Davies, J. R. J. Downey, D. J. Frurip, R. A. McDonald, and A. N. Syverud, *Journal of Physical and Chemical Reference Data* **14**, (1985), Supplement No. 1, JANAF Thermochemical Tables, Third Edition.
- ³⁴D. Sergeev, D. Kobertz, and M. Müller, *Thermochimica Acta* **606**, 25 (2015).
- ³⁵M. P. Tosi and F. G. Fumi, *Journal of Physics and Chemistry of Solids* **25**, 45 (1964).
- ³⁶D. J. Adams and I. R. McDonald, *Journal of Physical Chemistry C: Solid State Physics* **7**, 2761 (1974).
- ³⁷A. J. Thakkar, *The Journal of Chemical Physics* **81**, 1919 (1984).
- ³⁸J. E. Mayer, *The Journal of Chemical Physics* **1**, 270 (1933).
- ³⁹J. Alejandro, D. J. Tildesley, and G. A. Chapela, *Molecular Physics* **85**, 651 (1995).
- ⁴⁰J. L. Rivera, C. McCabe, and P. T. Cummings, *Phys. Rev. E* **67**, 011603 (2003).
- ⁴¹Y. Liu, T. Lafitte, A. Z. Panagiotopoulos, and P. G. Debenedetti, *AIChE Journal* **59**, 3514 (2013).
- ⁴²B. C. Knott, V. Molinero, M. F. Doherty, and B. Peters, *Journal of the American Chemical Society* **134**, 19544 (2012), pMID: 23148735.
- ⁴³H. M. Manzanilla-Granados, H. Saint-Martín, R. Fuentes-Azcatl, and J. Alejandro, *The Journal of Physical Chemistry B* **119**, 8389 (2015), pMID: 26036707.
- ⁴⁴J. Kolafa, *The Journal of Chemical Physics* **145**, 204509 (2016).
- ⁴⁵J. R. Espinosa *et al.*, *The Journal of Chemical Physics* **145**, 154111 (2016).
- ⁴⁶G. E. Norman and V. S. Filinov, *High Temperature (USSR)* **7**, 216 (1969).
- ⁴⁷D. Frenkel and B. Smit, *Understanding Molecular Simulation* (Elsevier, London, 2002).
- ⁴⁸A. Z. Panagiotopoulos, *Molecular Physics* **61**, 813 (1987).
- ⁴⁹M. Mehta and D. A. Kofke, *Chemical Engineering Science* **49**, 2633 (1994).
- ⁵⁰M. R. Hitchcock and C. k. Hall, *Journal of Chemical Physics* **110**, 11433 (1999).
- ⁵¹E. A. Mastny and J. J. de Pablo, *Journal of Chemical Physics* **122**, 124109 (2005).
- ⁵²S. Boothroyd, A. Kerridge, A. Broo, D. Buttar, and J. Anwar, *Physical Chemistry Chemical Physics* **20**, 20981 (2018).
- ⁵³F. Moučka, M. Lísal, J. Škvor, J. Jirsák, I. Nezbeda, and W. R. Smith, *The Journal of Physical Chemistry B* **115**, 7849 (2011), pMID: 21627127.
- ⁵⁴J. W. Cahn, *Acta Metallurgica* **37**, 773 (1989).
- ⁵⁵J. W. Cahn and F. Lärché, *Acta Metallurgica* **30**, 51 (1982).
- ⁵⁶D. A. Kofke and E. D. Glandt, *Molecular Physics* **64**, 1105 (1988).
- ⁵⁷B. Widom, *The Journal of Chemical Physics* **39**, 2808 (1963).
- ⁵⁸P. Sindzingre, G. Ciccotti, C. Massobrio, and D. Frenkel, *Chemical Physics Letters* **136**, 35 (1987).
- ⁵⁹N. L. Allan, G. D. Barrera, M. Y. Lavrentiev, I. T. Todorov, and J. A. Purton, *Journal of Materials Chemistry* **11**, 63 (2001).
- ⁶⁰J. Anwar, *ATOMH: An Object-Oriented Molecular Simulation Toolkit*, 1995.
- ⁶¹S. Plimpton, *Journal of Computational Physics* **117**, 1 (1995).
- ⁶²I. T. Todorov, W. Smith, and M. T. Dove, *Journal of Materials Chemistry* **16**, 1911 (2006).
- ⁶³L. Vegard, *Zeitschrift für Physik* **5**, 17 (1921).
- ⁶⁴A. Datta and C. Gopikrishnan, *AIP Advances* **2**, 12131 (2012).
- ⁶⁵J. Anwar, D. Frenkel, and M. G. Noro, *Journal of Chemical Physics* **118**, 728 (2003).
- ⁶⁶J. L. Aragones, E. Sanz, and C. Vega, *Journal of Chemical Physics* **136**, 244508 (2012).
- ⁶⁷B. Sadigh, P. Erhart, A. Stukowski, A. Caro, E. Martinez, and L. Zepeda-Ruiz, *Physical Review B - Condensed Matter and Materials Physics* **85**, 1 (2012).
- ⁶⁸J. Kim, T. Keyes, and J. E. Straub, *Journal of Chemical Physics* **132**, 224107 (2010).
- ⁶⁹E. A. Guggenheim, *Journal of Chemical Physics* **13**, 253 (1945).